Journal of Quantitative Spectroscopy & Radiative Transfer 243 (2020) 106816

Contents lists available at ScienceDirect

Journal of Quantitative Spectroscopy & Radiative Transfer

journal homepage: www.elsevier.com/locate/jqsrt

# Reflection and transmission by large inhomogeneous media. Validity of born, rytov and beam propagation methods

Patrick C. Chaumet [a,*], Anne Sentenac [a], Ting Zhang [b]

[a] Aix Marseille Univ, CNRS, Centrale Marseille, Institut Fresnel, Marseille, France
[b] College of Information Science and Electronic Engineering (ISEE), Zhejiang University, Zhejiang Provincial Key Laboratory of Information Processing, Communication and Networking (IPCAN), Hangzhou 310027, China

ARTICLE INFO

*Article history:*
Received 30 September 2019
Revised 20 December 2019
Accepted 24 December 2019
Available online 26 December 2019

*Keywords:*
Scattering
Discrete dipole approximation
Beam propagation method
Rytov approximation
Born approximation

ABSTRACT

The ability to model the backward and forward scattering by large inhomogeneous samples is of major importance especially for computational imaging applications. Unfortunately, when the sample dimensions exceed hundreds of wavelengths, a rigorous solving of the Maxwell Equations becomes difficult. In this work, we compare the scattered field estimated by a rigorous Maxwell equation solver, based on the discrete dipole approximation, with that given by several approached methods, Rytov, Born and a revisited Beam Propagation Method. We show on many examples, that BPM outperforms all the other techniques and accurately handles field distortion and moderate multiple scattering.



## 1. Introduction

The last fifteen years have seen the rise of several optical imaging techniques in which the three-dimensional inhomogeneous permittivity is reconstructed numerically from measurements of the field (or intensity) reflected or transmitted by the sample [1–6] under various illuminations. Their increased resolution and their ability to correct for aberrations and provide quantitative information make them an interesting alternative to classical analogical microscopes. In particular, they have appeared as a promising tool for label-free imaging of cells and biological tissues in the context of medical screening [3,6,7].

All these computational imaging techniques are based on a light-matter interaction model which links the measured reflected or transmitted field to the sample characteristics. For weakly contrasted biological specimen, most studies have focused on the Born or Rytov approximations and, more recently, on the Beam Propagation Method. Now, although these models have been developed a long time ago, their formulation is not always adapted to the imaging problem [8]. In particular, neither the Rytov nor the Beam Propagation Method have been considered when imaging in the reflection configuration (which corresponds to Optical Coherence Tomography and its numerous avatars). In addition, the accuracy of these models for biological applications have never been investigated due to the lack of reference methods. Indeed, the size of the samples (at least hundreds of wavelengths for biological tissues [6] and the multiscale and random nature of the permittivity inhomogeneities [9] make the rigorous modeling of the light propagation within these media particularly difficult.

In this work, we first show in a unified way how the Rytov, Born and Beam Propagation methods can be used to estimate the vectorial reflected and transmitted field in an imaging experiment. Then, using the discrete dipole approximation method as a reference for solving rigorously the Maxwell Equations, we analyze their accuracy on samples made of random medium with increasing thickness and varying correlation lengths and permittivity variance based on the values of biological specimen.

## 2. Theory

### 2.1. Rigorous model

We consider a sample described by its relative permittivity $\varepsilon(\mathbf{r}) = n^2(\mathbf{r})$ that is illuminated by a monochromatic incident field with wavenumber $k_0$, $\boldsymbol{E}_{\rm inc}$. The electric field satisfies the Lippmann-Schwinger equation,

$$\mathbf{E}(\mathbf{r}) = \mathbf{E}_{\rm inc}(\mathbf{r}) + k_0^2 \int_\Gamma \overline{\mathbf{G}}(\mathbf{r},\mathbf{r}')\chi(\mathbf{r}')\mathbf{E}(\mathbf{r}')\mathrm{d}\mathbf{r}'. \quad (1)$$

where $\Gamma$ is the domain where the dielectric contrast $\chi = \varepsilon - 1$ is non-zero, and $\overline{\mathbf{G}}$ is the Dyadic Green's function solution of

$$\nabla \times \nabla \times \overline{\mathbf{G}}(\mathbf{r},\mathbf{r}') - k_0^2 \overline{\mathbf{G}}(\mathbf{r},\mathbf{r}') = \delta(\mathbf{r},\mathbf{r}')\bar{\mathbf{I}}, \quad (2)$$

* Corresponding author.
*E-mail address:* patrick.chaumet@fresnel.fr (P.C. Chaumet).

https://doi.org/10.1016/j.jqsrt.2019.106816
0022-4073/

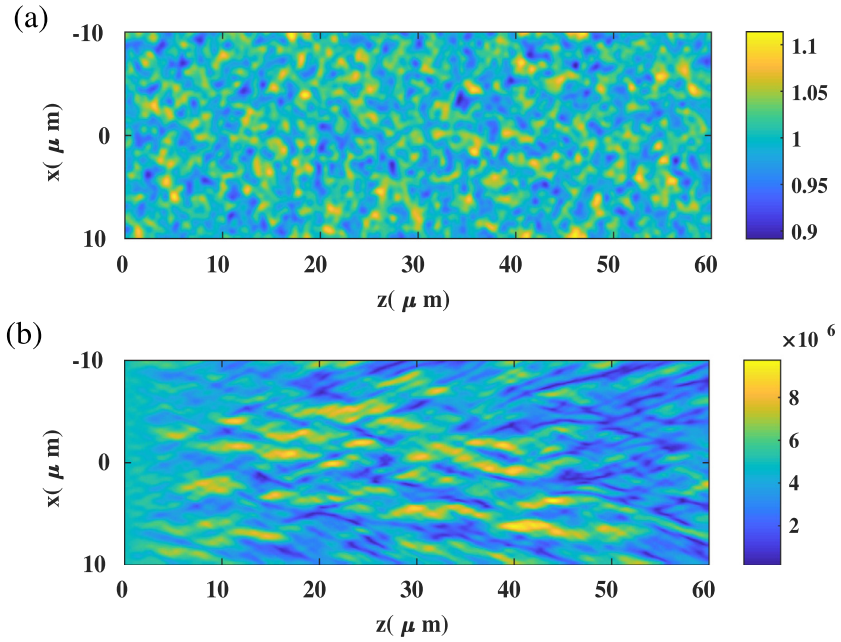


**Fig. 1.** (a) Map of the random relative permittivity with $l_c = 3\lambda$, $\sigma = 0.05$ and $L = 60$ $\mu$m. (b) Intensity of the macroscopic field inside the sample calculated rigorously with the DDA.

that satisfies out-going boundary condition. One can notice that the Green function is singular, hence the quadrature should be performed with precautions as it is detailed in Refs. [10,11]. In our case we treat the singularity as Draine in Ref. [12] to satisfy the optical theorem. We introduce the scattered field as $\mathbf{E} - \mathbf{E}_{\rm inc}$ and the scattered far-field in the direction $\hat{\mathbf{k}}$ as,

$$\mathbf{e}(\mathbf{k}) = k_0^2\Big[1 - \hat{\mathbf{k}}\hat{\mathbf{k}}.\Big]\mathcal{F}_{3D}[\chi\mathbf{E}](\mathbf{k}), \tag{3}$$

where $\mathcal{F}_{3D}[f](\mathbf{k}) = \frac{1}{8\pi^3}\int f(\mathbf{r})\exp(-i\mathbf{k}.\mathbf{r})\mathrm{d}\mathbf{r}$ is the three dimensional Fourier transform and $\mathbf{k} = k_0\hat{\mathbf{k}}$ and $\hat{\mathbf{k}}$ is the unit vector in the scattering direction. Eq. (3) shows how the field scattered by the sample *in any backward or forward direction* can be obtained once the field $\boldsymbol{E}$ inside the sample is known.

The field inside $\Gamma$ can be estimated rigorously by solving the self-consistent equation Eq. (1). This approach corresponds to the Discrete Dipole Approximation also called coupled dipole method and is based on a Volume Integral Method, see Ref. [11] for more details and appendix A. Eq. (1) is transformed into a linear system by discretizing $\Gamma$ into cubic sub-units over which the field and dielectric contrast are assumed to be constant [13]. A conjugate gradient scheme is then used to estimate the field at each subunit. The absence of perfectly matched layers and the restriction of the meshing to the dielectric contrast support make the DDA [12,14] particularly adapted to the free-space scattering of moderately large samples [15] but it requires an important computation time. To have more details on the capabilities and limitations of DDA, the readers can read Ref. [16].

For applications where many direct problems need to be solved, as in computational imaging, or when the samples are too big, an approximate estimation of the field inside $\Gamma$ is often used.

### 2.2. Born approximation at order 0 and 1

The simplest approximation for $\boldsymbol{E}$ is given by the zero order of the Born series (Born) obtained from Eq. (1), $\boldsymbol{E}(\boldsymbol{r}) \approx \boldsymbol{E}_{\rm inc}(\boldsymbol{r})$. It is valid for samples that weakly perturb the incident field (small permittivity contrast and small size compared to the wavelength). This approximation is used in many computational tomography technique as it provides a one to one correspondence between the scattered field, Eq. (3), and the 3D Fourier coefficient of the dielectric contrast [17,18].

To improve the estimation of the internal field, one can take the first order of the Born series (Born 1),

$$\mathbf{E}(\mathbf{r}) \approx \mathbf{E}_{\rm inc}(\mathbf{r}) + k_0^2\int_\Gamma \overline{\mathbf{G}}(\mathbf{r},\mathbf{r}')\chi(\mathbf{r}')\mathbf{E}_{\rm inc}(\mathbf{r}')\mathrm{d}\mathbf{r}', \tag{4}$$

which is computationally more expensive but accounts for some multiple scattering.

### 2.3. Rytov approximation

A more sophisticated model, the Rytov approximation, has been proposed to describe the field propagation in samples that are weakly contrasted but with dimensions that can be large compared to the wavelength [19–21]. In this model the $\beta = (x, y, z)$ component of the field reads $E^\beta(\mathbf{r}) \approx E^\beta_{\rm inc}(\mathbf{r})e^{\Phi^\beta(\mathbf{r})}$ with

$$\Phi^\beta(\mathbf{r}) = \left[k_0^2\int_\Gamma \overline{\mathbf{G}}(\mathbf{r},\mathbf{r}')\chi(\mathbf{r}')\mathbf{E}_{\rm inc}(\mathbf{r}')\mathrm{d}\mathbf{r}'\right]^\beta / E^\beta_{\rm inc}(\mathbf{r}). \tag{5}$$

Note that the Rytov computation time is the same as that of the Born approximation at first order.

### 2.4. Beam propagation method

The beam propagation method (BPM) has been developed to describe the propagation of the field inside inhomogeneous media in which forward scattering is dominant, Refs. [22–24]. Assuming that the medium is illuminated by a collimated beam propagating towards positive $z$ and neglecting backward scattering, the field at plane $z = z_0 + \delta z$, $\mathbf{E}_{z_0+\delta z}(x, y)$, is deduced from the knowledge of the field at plane $z = z_0$, $\mathbf{E}_{z_0}(x, y)$ via,

$$\mathbf{E}_{z_0+\delta z}(x,y) \approx e^{ik_0 n(x,y,z_0+\delta z)\delta z}\mathcal{F}_{2D}^{-1}\Big[\mathcal{F}_{2D}[\mathbf{E}_{z_0}](k_x,k_y)e^{-i(k_0-k_z)\delta z}\Big], \tag{6}$$

where $\mathcal{F}_{2D}$ is the 2D Fourier transform in the $(x, y)$ plane and $k_z = \sqrt{k_0^2 - k_x^2 - k_y^2}$. If $\Gamma$ is included in the $z > 0$ half-space, The field at $z = 0$ is taken equal to the incident field. Hereafter, we denote by Born0, Born1, Rytov and BPM the different approximations

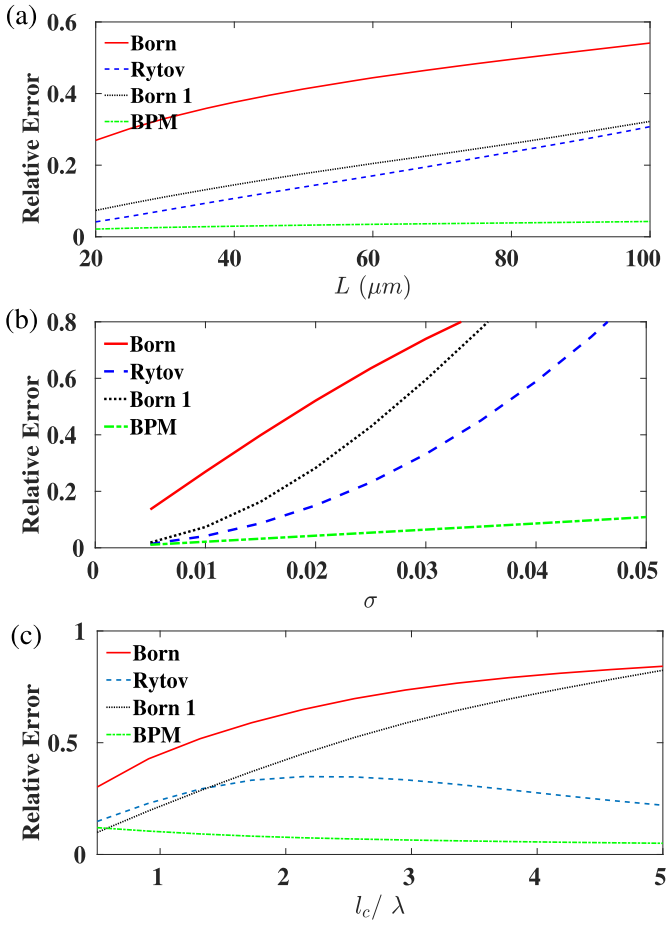


**Fig. 2.** (a) Relative error on the internal field for a random sample of width $l = 20\ \mu$m, $\sigma = 0.01$ and $l_c = 3\lambda$ as a function of the length $L$. (b) same as (a) with $L = 20\ \mu$m and $l_c = 3\lambda$ as a function of $\sigma$; (c) same as (a) with $\sigma = 0.03$ and $L = 20\ \mu$m as a function of $l_c$.

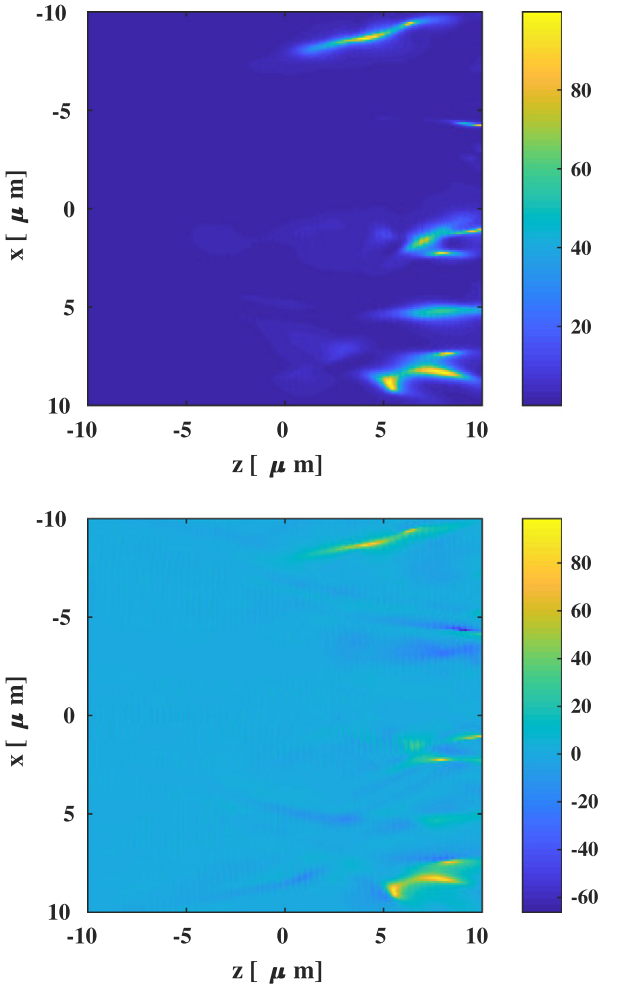


**Fig. 3.** (a) Density of energy in the cross polarization in per cent for a random sample of size $l = L = 20\ \mu$m, $\sigma = 0.05$ and $l_c = 3\lambda$. (b) For the same sample map of the relative error in per cent for the field modulus between DDA and BPM.

for the field inside $\Gamma$. Note that contrary to Born1, Born0, Rytov and BPM models are not able to account for any cross-polarization, if $E^{\beta}_{\rm inc}(\mathbf{r}) = 0$ then $E^{\beta}(\mathbf{r}) = 0$. All the methods used in this article have been implemented by meshing $\Gamma$ in cubit sub-units of side 100 nm Refs. [25,26].

## 3. Numerical results

### 3.1. Description of the geometry

The validity of the models is studied on scattering objects with varying contrast and varying lengthscales to approach the multiscale nature and the composition diversity of biological samples [9]. We consider a cuboid of random medium with transverse dimensions $l \times l$ and thickness along $z$, $L$. The cuboid of random medium is placed in an index-matching background to limit the influence of the cuboid boundaries on the scattered field and focus on the role of the correlation length and index variance of the random medium. The relative permittivity of the random medium is a Gaussian distributed random variable of mean $\varepsilon_{\rm bg}$ and variance $\sigma^2$, with a Gaussian correlation function, [27],

$$\left\langle \varepsilon(\mathbf{r}), \varepsilon(\mathbf{r}') \right\rangle = \varepsilon_{\rm bg}^2 + \sigma^2 \exp\left( -\frac{\|\mathbf{r} - \mathbf{r}'\|^2}{l_c^2} \right), \tag{7}$$

where $< >$ stands for the ensemble average and $l_c$ is the correlation length, see Fig. 1(a) for an illustration of the sample. The cuboid is embedded into the homogeneous background of permittivity $\varepsilon_{\rm bg}$. Increasing the thickness $L$ from a few microns to hundreds of microns, permits to investigate the accuracy of the models when most of the ballistic light disappears. In the following, the samples are illuminated by an incident plane wave linearly polarized along $y$ and propagating along $z$ with wavelength $\lambda = 632.8$ nm and the transverse width of the cuboid is kept fixed to $20 \times 20\,\mu$m$^2$ for the rigorous computation to be tractable. The meshsize is about 100 nm which gives a good precision for the DDA as shown in the appendix A. To illustrate the complexity of the scattering inside these objects, we plot in Fig. 1(b) the field modulus obtained with the rigorous DDA inside the cuboid of random medium depicted in Fig. 1(a). It is seen that the permittivity inhomogeneities perturbs significantly the illumination, the intensity resembling a speckle after $10\,\mu$m of propagation inside the sample.

### 3.2. Accuracy of born, rytov and BPM for modeling the field inside the sample

To analyze quantitatively the accuracy of the different field approximations, we introduce the relative error on the internal field, $\mathrm{Err}_{\rm nf}$, with obvious notations,

$$\mathrm{Err}_{\rm nf} = \frac{\int_\Gamma \left\| \mathbf{E}_{\rm rig}(\mathbf{r}) - \mathbf{E}_{\text{approx. method}}(\mathbf{r}) \right\| \mathrm{d}\mathbf{r}}{\int_\Gamma \left\| \mathbf{E}_{\rm rig}(\mathbf{r}) \right\| \mathrm{d}\mathbf{r}}. \tag{8}$$

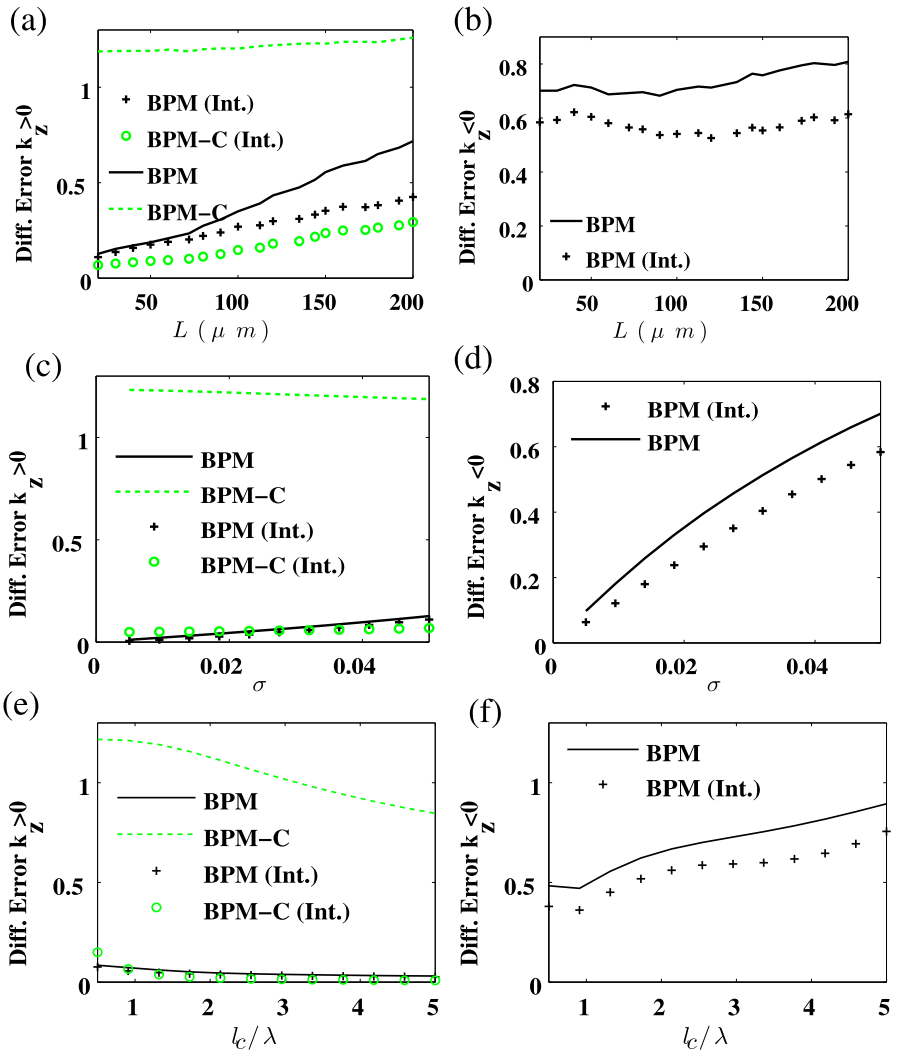


**Fig. 4.** Error on the scattered far-field with a width $l = 20$ $\mu$m and increasing (a), (b) thickness $L$ with $\sigma = 0.05$ and $l_c = 3\lambda$; (c), (d) $\sigma$ for $l_c = 3\lambda$ and $L = 20$ $\mu$m; (e), (f) $l_c$ with $\sigma = 0.05$ and and $L = 20$ $\mu$m. (a), (c) and (e) for $k_z > 0$ (b), (d) and (f) for $k_z < 0$. The label BPM-C indicates that the transmitted field as been estimated using the free-space propagator while BPM indicates that it has been estimated using Eq. (3). The errors on the far-field are calculated using the complex field values, except when Int is added to the label, in which case the error is calculated using the intensity values.

In Figs. 2(a–c) we plot the errors on the internal field $\mathrm{Err}_{\mathrm{nf}}$ for the Born zero and first order, Rytov and BPM models as a function of the thickness $L$ of the sample, the correlation length $l_c$ and the permittivity variance $\sigma$. It is observed on several realizations of the random cuboid that, whatever the parameters of the random medium, BPM outperforms all the other methods. Interestingly, if, as expected, BPM is well adapted to random medium with large $l_c/\lambda$ for which the forward scattering is dominant, it is also accurate when $l_c$ is inferior to $\lambda$, when scattering is less forward-peaked. Thus, BPM is a good approach for simulating the propagation in multiscale media such as biological tissues in which large medium fluctuations co-exist with small structures. Its computation time being similar or smaller than that of Rytov and Born 1 (for $l = L = 20$ $\mu$m, $\sigma = 0.05$, $l_c = 3\lambda$, BPM time is about 20 s while the rigorous calculation time is 450 s), it should always be preferred to the latter, see Table 1.

As previously remarked, BPM does not account for any cross polarization. We plot in Fig. 3(a) the map of density of energy in the cross polarization divided by the total density of energy in per cent for $\sigma = 0.05$, $l_c = 3\lambda$ and $L = 20$ $\mu$m. It is observed that the cross polarization increases with the penetration of the beam in the medium. In Fig. 3(b), the relative error in percent between the DDA and BPM fields is plotted. We notice that the error is maximum when the cross polarization is important. This analysis suggests that BPM inaccuracy lays in the overlooking of the cross polarization (which is a marker of strong multiple scattering).

We now turn to a more precise analysis of the accuracy of BPM in the context of imaging applications and focus on the ability of BPM to simulate the reflected and transmitted far-field which are the only data that are accessible experimentally.

**Table 1**
Computation time required to estimate the internal field in a sample of size $20 \times 20 \times 20\,\mu\mathrm{m}^3$ with random permittivity, variance $\sigma = 0.05$ and correlation length $l_c = 3\lambda$. The processor used is an Intel(R) Xeon(R) CPU E5-2687W at 3.40GHz.

| Method | rigorous | B | B1 | R | BPM |
|---|---|---|---|---|---|
| Time (s) | 450 | 0.5 | 19 | 18 | 12 |

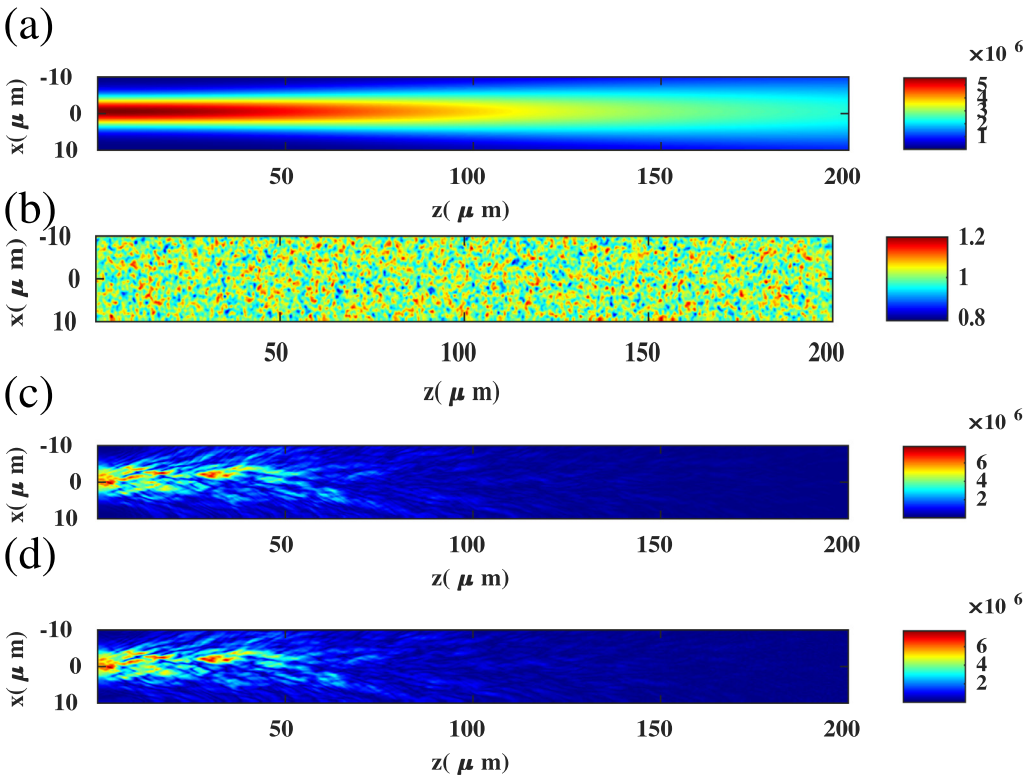


**Fig. 5.** (a) Incident field propagating in the homogeneous background. It is a Gaussian beam, at $\lambda = 632.8$ nm, with waist $6\,\mu$m, linearly polarized that is focused at the entrance of the sample box. (b) Map of the relative permittivity with $l_c = 3\lambda$, $\sigma = 0.05$ and $L = 200\ \mu$m. Macroscopic field inside the sample calculated (c) rigorously with the DDA and (d) with the BPM.

### *3.3. Accuracy of BPM for estimating the reflected and transmitted scattered field*

We define the relative error between the rigorous scattered far-field and the BPM scattered in the same way as the relative error on the internal field,

$$\mathrm{Err}_{\mathrm{ff}} = \frac{\int \left\| \mathbf{e}_{\mathrm{rig}}(\hat{\mathbf{k}}) - \mathbf{e}_{\mathrm{approx.\ method}}(\hat{\mathbf{k}}) \right\| \mathrm{d}\Omega}{\int \left\| \mathbf{e}_{\mathrm{rig}}(\hat{\mathbf{k}}) \right\| \mathrm{d}\Omega}, \tag{9}$$

where the integral is performed over the directions of observation in $2\pi$ str with $k_z > 0$ for the transmission configuration and $k_z < 0$ for the reflection configuration. This relative error $\mathrm{Err}_{\mathrm{ff}}$ depends on both the amplitude and phase of the far-field as measured in holographic experiments [1,2,4,5,28]. In certain experiments, however, such as ptychography [3,29], we have access only to the far-field intensity $I = |\mathbf{e}|^2$ and a relative error on the intensity similar to $\mathrm{Err}_{\mathrm{ff}}$ is more pertinent.

$$\mathrm{Err}_{\mathrm{Int.}} = \frac{\int \left| I^{\mathrm{sca}}(\hat{\mathbf{k}}) - I^{\mathrm{sca}}_{\mathrm{approx.\ method}}(\hat{\mathbf{k}}) \right| \mathrm{d}\Omega}{\int I^{\mathrm{sca}}(\hat{\mathbf{k}}) \mathrm{d}\Omega}. \tag{10}$$

In computational microscopy, accurate reconstructions have been obtained when the relative error between the noisy experimental data and the theoretical field of the target was above 0.8 [1,2]. Thus, an error of 0.8 for an approximate model is *a priori* acceptable for this kind of application.

Several options are possible for estimating the scattered far-field $\boldsymbol{e}$ once the internal field $\boldsymbol{E}$ is known. It can be calculated by summing the field radiated by the induced polarization within the sample following Eq. (3). It can also be computed by propagating in free space the total field minus the incident field obtained at the entrance plane or the exit plane of the sample. These two approaches give the same results when Maxwell Equations are rigorously solved but differ when approximations are used.

In classical BPM, the transmitted far-field is obtained through propagation in free-space of the field at the sample exit plane (BPM-C). In this work, we also estimate the transmitted far-field from the knowledge of the BPM internal field using Eq. (3) (BPM). In Fig. 4, the label BPM-C indicates that the transmitted field as been estimated using the free-space propagator while the label BPM indicates that it has been estimated using Eq. (3). The errors on the far-field are calculated using the complex field values, except when Int is added to the label, in which case the error is calculated using the intensity values.

Fig. 4 (a,c,e) display the transmitted far-field relative error of these different estimations as a function of thickness $L$, permittivity variance, and correlation length, respectively. It is observed that the calculation of the transmitted far-field through the radiation of the induced polarization, Eq. (3) (BPM curves), is much more accurate than the free-space propagation (BPM-C curves) for estimating the phase of the field and (not shown) the amplitude far from the specular direction. Since this approach requires only minor additional computational time, it should be preferred in general to the classical free-space propagation. Its relative error is remarkably low (below 0.5) for most of the parameters. Note that the errors on the intensity of BPM and BPM-C are close to each other, meaning that the inaccuracy of the classical propagation scheme affects mainly the phase of the transmitted beam.

We now turn to the analysis of the reflected far-field. In classical BPM, the reflected field is generally not calculated (except with some advanced implementations which are significantly more complex than the one presented here [30]). Here, we simply es-

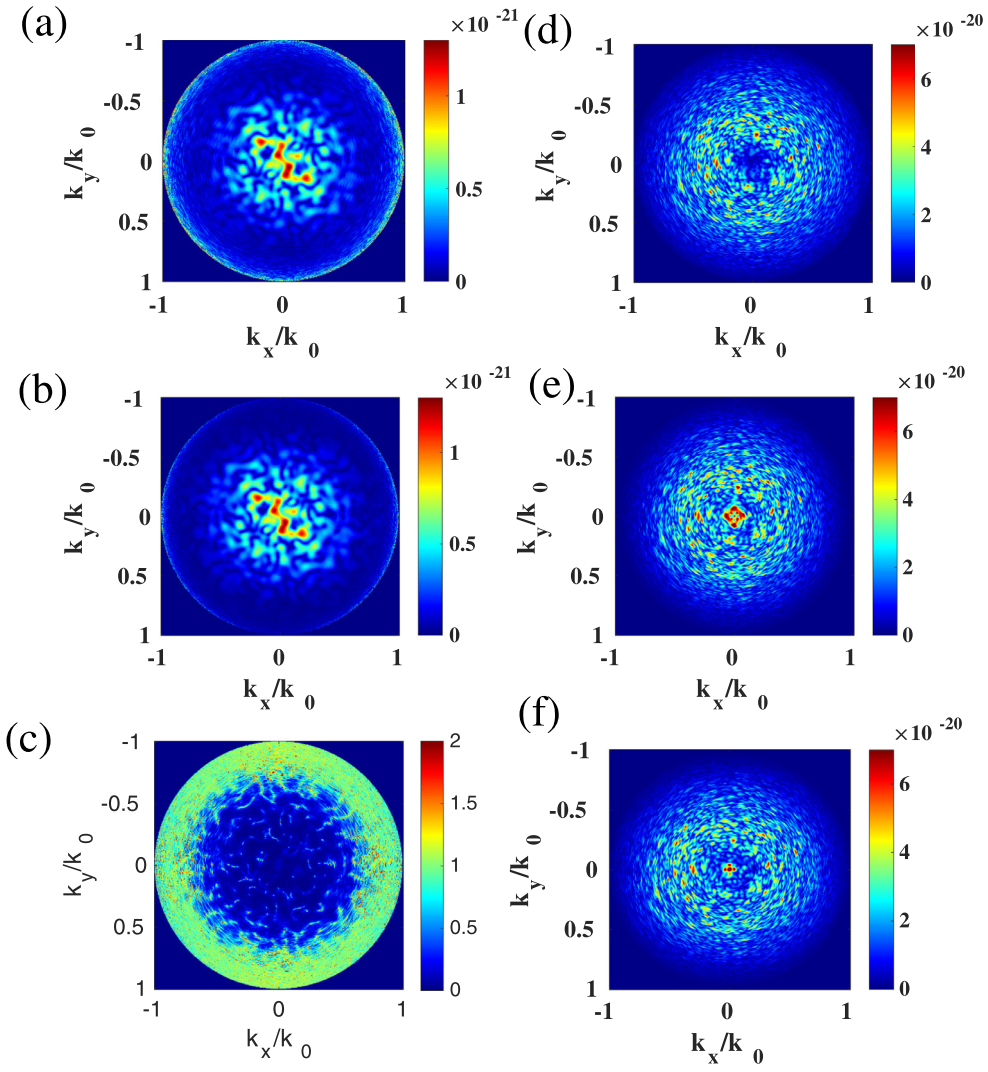


**Fig. 6.** Map of the scattered field modulus in reflection for (a) DDA and (b) BPM, (c) local error between (a) and (b) computed for each direction of observation as $\| \boldsymbol{e}_{\text{rig}} - \boldsymbol{e}_{\text{BPM}} \| / \| \boldsymbol{e}_{\text{rig}} \|$. Total diffracted field in transmission for (d) DDA, (e) BPM, and (f) BPM-C.

timate the reflected far-field from the BPM internal field using Eq. (3). Fig. 4(b,d,f) display its relative error as a function of thickness, permittivity variance, and correlation length. The higher error in reflection than in transmission leads one to believe that BPM does not estimate the reflected field as accurately as the transmitted one. Actually, this discrepancy stems mainly from the fact that, due to the absence of any specular reflected field, the scattered field at high angles weights more heavily on the total reflected power than on the total transmitted one. Now, BPM accuracy on the scattered field is about the same in reflection and transmission and it deteriorates with increasing angles. Interestingly, the reflection error does not increase with the thickness of the sample $L$. It was observed (not shown) that the reflected field depended basically on the first 60 µm of the random medium. This thickness corresponds roughly to the propagation length after which the internal field becomes negligible due to the leakage through the edges of the elongated cuboid. Actually, because of this leakage, the reflected power never exceeds 1%. Thus, forward propagation remains dominant in the sample (even though the ballistic light is significantly damped) which explains the accuracy of BPM. Additional simulations (not shown) indicated that when the reflected power exceeds a few percents, the error on the BPM field increases drastically.

Actually, the leakage at the boundaries of the cuboid is not realistic. In practice, the sample and the illuminating field extend over hundreds of microns in the transverse plane. To model such a configuration, a possible approach, inspired from the study of rough surfaces scattering [31], consists in decomposing the wide incident beam into a sum of translated Gaussian beams with small waist and the random medium into an assembly of cuboids with small transverse dimensions. For this decomposition to be valid, the field obtained for a small waist Gaussian beam, should be negligible at the transverse boundaries of the cuboid. In the last example, we consider the thickest cuboid ($L = 200$ $\mu$m, $l = 20$ $\mu$m) with $\sigma = 0.05$ and $l_c = 3\lambda$ depicted in Fig. 5(b). A Gaussian beam [32] with waist $6\,\mu$m and polarized along $y$, illustrated in Fig. 5(a), is focused at the entrance of the sample. Fig. 5(c,d) display the modulus of the field inside the sample calculated with the rigorous DDA solver and with the BPM. As expected, during propagation, the field spreads in the transverse directions until it reaches the boundaries of the cuboid. We estimate the maximal depth of the random medium for which the specific transverse dimensions of the cuboid are sufficient to simulate an infinitely extended sample to be about $40\,\mu$m. The scattering, distortion and leakage of the field are accurately retrieved by the BPM.

The similarity between the rigorous and approximate estimations are retrieved in the far-field study. In Fig. 6(a,b), we compare the DDA and BPM reflected far-field and observe that the speckle features are accurately reproduced. The main discrepancies between BPM and DDA are found near the edge of the numerical aperture as seen in Fig. 6(c).

Fig. 6(d) displays the rigorous total transmitted far-field (where the incident Gaussian beam has been added to the scattered field) which corresponds to the field that would actually be measured in an experiment. We observe speckle like features outside the forward direction which are globally recovered by both the BPM and BPM-C. We also observe an important damping of the ballistic light, stemming from the leakage at the cuboid boundaries, which corresponds to the destructive interference between the scattered field and the incident beam. This behavior is more difficult to obtain as it requires a precise estimation of the scattered field phase. In this case, the BPM using the radiation equation, Eq. (3), is better suited, as previously noted in Fig. 4(a,c,e), but still insufficient.

## 4. Conclusion

In conclusion, we have shown that, BPM outperforms significantly Born and Rytov approximations for simulating the field inside biological-like samples. Once the internal field is known, the far-field radiation equation permits to estimate the scattered field in any direction, in particular in reflection. We have observed that BPM yielded accurate results as long as the reflected power remained smaller than a few percents of the incident one. This study paves the way towards imaging of complex samples that strongly distort and scatter light.

## Appendix A. DDA

In this work, the code IF-DDA [26] was used to compute the field with DDA and BPM as both options are available. The integral equation Eq. (1) is discretized as,

$$\mathbf{E}(\mathbf{r}_i) = \mathbf{E}_{\rm inc}(\mathbf{r}_i) + \sum_{j=1}^{N} \mathbf{G}(\mathbf{r}_i, \mathbf{r}_j)\alpha(\mathbf{r}_j)\mathbf{E}(\mathbf{r}_j), \tag{A.1}$$

where the polarizability reads as [12]

$$\alpha_0(\mathbf{r}_j) = \frac{3d^3}{4\pi}\frac{\varepsilon(\mathbf{r}_j)-1}{\varepsilon(\mathbf{r}_j)+2}, \tag{A.2}$$

$$\alpha(\mathbf{r}_j) = \frac{\alpha_0(\mathbf{r}_j)}{1-\frac{2}{3}ik^3\alpha_0(\mathbf{r}_j)}. \tag{A.3}$$

The field inside the object is obtained by solving iteratively the linear system represented by Eq. (A.1) using GPBICG [33,34].

To check the precision of our rigorous solver (DDA) we considered a sphere in vacuum with a radius $a = 10\ \mu$m and a refractive index which varies from 1.01 to 1.15 and a wavelength of illumination $\lambda = 632.8$ nm. The index variation has been chosen to match that of the random media under study. We compared the extinction cross section, [12] asymmetric factor [12] and optical force [35,36] obtained with Mie theory to that given by the DDA with a meshsize of 100 nm.

In Fig. A.1 we plot the relative error in per cent between the DDA and the Mie theory. We see that for the three parameters studied the relative error remains always below that 4%, hence the precision of the DDA with this discretization is enough to serve as a reference for the other approximated methods.

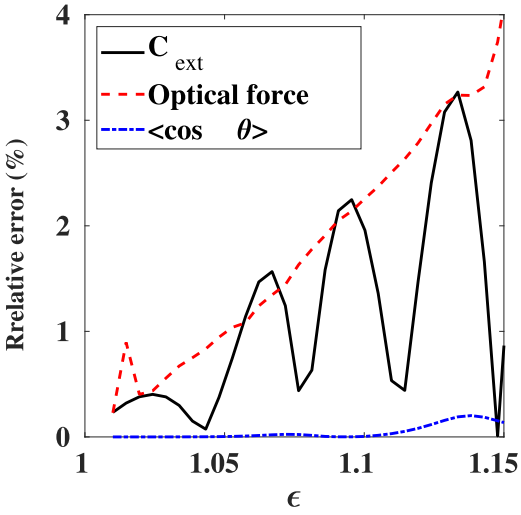


**Fig. A.1.** Relative error for the extinction cross section, asymmetrical factor and optical force between Mie theory and DDA versus the relative permittivity for a sphere of radius $a = 10\ \mu$m, with $\lambda = 632.8$ nm and meshsize of 100 nm for the DDA.

## References


[1] Zhang T, Ruan Y, Maire G, Sentenac D, Talneau A, Belkebir K, et al. Full-polarized tomographic diffraction microscopy achieves a resoluti on about one–fourth of the wavelength. Phys Rev Lett 2013;111:243904.
[2] Zhang T, Godavarthi C, Chaumet PC, Maire G, Giovannini H, Talneau A, Allain M, Belkebir K, Sentenac A. Far-field diffraction microscopy at λ/10 resolution. Optica 2016;3(6):609–12.
[3] Greenbaum A, Zhang Y, Feizi A, Chung P-L, Luo W, Kandukuri SR, Ozcan A. Wide-field computational imaging of pathology slides using lens-free on-chip microscopy. Science Translational Medicine 2014;6(267). 267ra175–267ra175.
[4] Badon A, Li D, Lerosey G, Boccara AC, Fink M, Aubry A. Smart optical coherence tomography for ultra-deep imaging through highly scattering media. Sci Adv 2016;2(11):e1600370.
[5] Choi W, Fang-Yen C, Badizadegan K, Oh S, Lue N, Dasari RR, Feld MS. Tomographic phase microscopy. Nat Methods 2007;4:717–19.
[6] Ahmad A, Shemonski ND, Adie SG, Kim H-S, Hwu W-MW, Carney PS, Boppart SA. Real-time in vivo computed optical interferometric tomography. Nat Photon 2013;6(7):444–8.
[7] Jin D, Zhou R, Yaqoob Z, So PTC. Tomographic phase microscopy: principles and applications in bioimaging. J Opt Soc Am B 2017;34(5):B64–77.
[8] Lim J, Ayoub AB, Psaltis D. High-fidelity optical diffraction tomography of multiple scattering samples. Light Sci Appl 2019;8:82.
[9] Glaser AK, Chen Y, Liu JTC. Fractal propagation method enables realistic optical microscopy simulations in biological tissues. Optica 2016;3(8):861–9.
[10] Lakhtakia A. Strong and weak forms of the method of moments and the coupled dipole method for scattering of time-harmonic electromagnetics fields. Int J Mod Phys C 1992;3:583–603.
[11] Yurkin MA, Hoekstra AG. The discrete dipole approximation: an overview and recent developments. J Quant Spect Rad Transf 2007;106:558–89.
[12] Draine BT. The discrete-dipole approximation and its application to interstellar graphite grains. Astrophys J 1988;333:848–72.
[13] Chaumet PC, Sentenac A, Rahmani A. Coupled dipole method for scatterers with large permittivity. Phys Rev E 2004;70. 036606–6.
[14] Draine BT, Flatau PJ. Discrete-dipole approximation for scattering calculations. J Opt Soc Am A 1994;11:1491–9.
[15] Yurkin MA, Maltsev VP, Hoekstra AG. The discrete dipole approximation for simulation of light scattering by particles much larger than the wavelength. J Quant Spect Rad Transf 2007;106:546–57.
[16] Yurkin MA, Hoekstra AG. The discrete-dipole-approximation code adda: capabilities and known lim itations. J Quant Spect Rad Transf 2011;112(13):2234–47.
[17] Lauer V. New approach to optical diffraction tomography yielding a vector equation of diffraction tomography and a novel tomographic microscope. J Microsc 2002;205:165–76.
[18] Wolf E. Three-dimensional structure determination of semi-transparent objects from holographic data. Opt Commun 1969;1:153–6.
[19] Habashy TM, Groom RW, Spies BR. Beyond the born and rytov approximations–a nonlinear approach to electromagnetic scattering. J Geophys Res [Solid Earth] 1993;98:1759–75.
[20] Carminati R. Phase properties of the optical near field. Phys Rev E 1997;55:R4901–4.
[21] Chen B, Stamnes JJ. Validity of diffraction tomography based on the first born and the first rytov approximations. Appl Opt 1998;37(14):2996–3006.

[22] Kamilov US, Papadopoulos IN, Shoreh MH, Goy A, Vonesch C, Unser M, Psaltis D. Learning approach to optical tomography. Optica 2015;2(6):517–22.
[23] Kamilov US, Papadopoulos IN, Shoreh MH, Goy A, Vonesch C, Unser M, Psaltis D. Optical tomographic image reconstruction based on beam propagation and sparse regularization. IEEE Transactions on Computational Imaging 2016;2(1):59–70.
[24] Roey JV, van der Donk J, Lagasse PE. Beam-propagation method: analysis and assessment. J Opt Soc Am 1981;71(7):803–10.
[25] Chaumet PC, Zhang T, Sentenac A. Fast far-field calculation in the discrete dipole approximation. J Quant Spect RadTransf 2015;165:88–92.
[26] Chaumet P.C., Sentenac A., Sentenac D.. the computations were done using the free software IFDDA. https://github.com/pchaumet/IF-DDA.
[27] Zhang T, Chaumet PC, Mudry E, Sentenac A, Belkebir K. Electromagnetic wave imaging of targets buried in a cluttered medium u sing a hybrid inversion-dort method. Inverse Probl 2012;28(12):125008.
[28] Ralston TS, Marks DL, Carney PS, Boppart SA. Interferometric synthetic aperture microscopy. Nat Phys 2007;3:129–34.
[29] Tian L, Waller L. 3D intensity and phase imaging from light field measurements in an led array microscope. Optica 2015;2(2):104–11.
[30] Rao H, Scarmozzino R, Osgood RM. A bidirectional beam propagation method for multiple dielectric interfaces. IEEE Photonics Technol Lett 1999;11(7):830–2.
[31] Saillard M, Maystre D. Scattering from random rough surfaces: a beam simulation method. J Optics 1988;19(4):173–6.
[32] Chaumet PC. Fully vectorial highly non paraxial beam close to the waist. J Opt Soc Am A 2006;23:3197–202.
[33] Tang J, Shen Y, Zheng Y, Qiu D. An efficient and flexible computational model for solving the mild slope equation. Coast Eng 2004;51:143–54.
[34] Chaumet PC, Rahmani A. Efficient iterative solution of the discrete dipole approximation for magneto-dielectric scatterers. Opt Lett 2009;34:917–19.
[35] Chaumet PC, Rahmani A, Nieto-Vesperinas M. Photonic force spectroscopy on metallic and absorbing nanoparticles. Phys Rev B 2005;71(4):045425.
[36] Chaumet PC, Rahmani A, Sentenac A, Bryant GW. Efficient computation of optical forces with the coupled dipole method. Phys Rev E 2005;72. 046708–6.